Chem Soc Rev

This article was published as part of the

In-situ characterization of heterogeneous catalysts themed issue

Guest editor Bert M. Weckhuysen

Please take a look at the issue 12 2010 table of contents to access other reviews in this themed issue

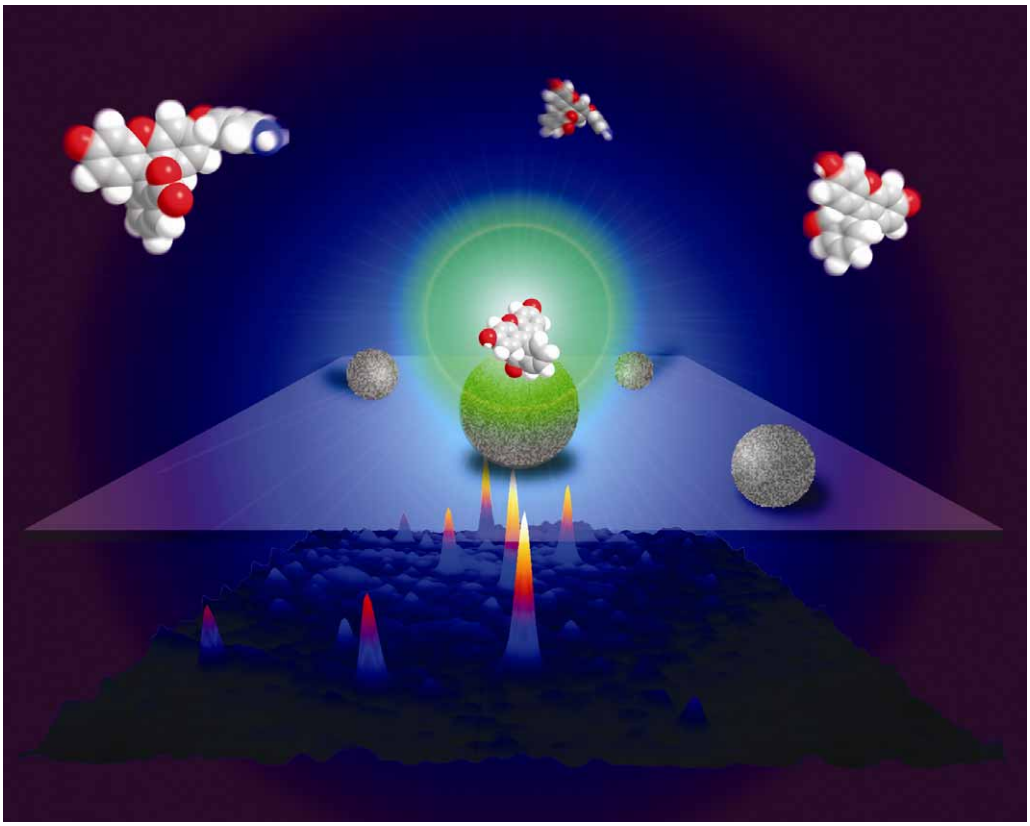

Chemical imaging of catalytic solids with synchrotron radiation†‡

Andrew M. Beale,* Simon D. M. Jacques and Bert M. Weckhuysen*

Received 27th August 2010
DOI: 10.1039/c0cs00089b

Heterogeneous catalysis is a term normally used to describe a group of catalytic processes, yet it could equally be employed to describe the catalytic solid itself. A better understanding of the chemical and structural variation within such materials is thus a pre-requisite for the rationalising of structure–function relationships and ultimately to the design of new, more sustainable catalytic processes. The past 20 years has witnessed marked improvements in technologies required for analytical measurements at synchrotron sources, including higher photon brightness, nano-focusing, rapid, high resolution data acquisition and in the handling of large volumes of data. It is now possible to image materials using the entire synchrotron radiative profile, thus heralding a new era of *in situ*/operando measurements of catalytic solids. In this *tutorial review* we discuss the recent work in this exciting new research area and finally conclude with a future outlook on what will be possible/challenging to measure in the not-too-distant future.

1. Introduction

Catalytic solids possess a 3D structure which is rarely uniform. These imperfections inevitably result in a heterogeneous surface containing various 'chemical sites' some of which may possess some sort of catalytic activity and others which do not. Importantly their type, number and distribution play a crucial role in determining the overall catalyst performance including both the activity and the selectivity. Therefore in order to effectively evaluate and characterise catalytic solids it is not always sufficient to simply perform single point measurements. A complete characterisation, requires that information be obtained at the atomic, nano, micron and millimetre scales over the entire 3D structure of the solid.[1,2]

Crucially a number of recent developments in the application of synchrotron radiation (SR) such as improved spectral brightness (3rd and 4th generation sources), focusing optics (*e.g.* sagittal focusing, Kirkpatrick–Baez lenses, Fresnel zone plates, refractive lenses), detector sensitivity (highly sensitive energy discriminating/pixelated detectors (*e.g.* Frelon, PILATUS)[3,4] and optical fibre megabit data transfer) and data handling software (batch data processing) has enabled the imaging of catalytic materials with SR ranging from IR up to γ-rays. To date there are approximately 40 active synchrotrons world-wide, many of which possess a number of beamlines for performing imaging experiments.

Inorganic Chemistry and Catalysis, Debye Institute for NanoMaterials Science, Sorbonnelaan 16, 3584 CA, Utrecht, The Netherlands. E-mail: A.M.Beale@uu.nl, B.M.Weckhuysen@uu.nl; Fax: 00 31 302511027; Tel: 00 31 302536815

† Part of the themed issue covering recent advances in the *in-situ* characterisation of heterogeneous catalysts.

‡ Electronic supplementary information (ESI) available: Version of Table 1 in which each station has a hypertext link taking the reader directly to the beamline's webpage or else to information concerning the beamline specifications. See DOI: 10.1039/c0cs00089b

Andrew M. Beale

Andrew M. Beale (35) was born in Beckenham (UK) and went on to read Chemistry at Sussex University followed by a PhD in 2003 from the Royal Institution of Great Britain/University College London. Since 2004 he has been based in the department of Inorganic Chemistry and Catalysis, Utrecht University, first as a post-doctoral fellow and subsequently (2009) as Assistant Professor in the group of Professor Bert M. Weckhuysen. His research interests lie in the studying of catalytic processes using in situ/operando spectroscopic and scattering methods.

Simon D. M. Jacques

Simon Jacques (39) read Biochemistry at Kings College London and went on to obtain an MSc and PhD in Crystallography from Birkbeck College, London. From 2003 to 2010 he worked as a post-doctoral research assistant at Birkbeck and University College London developing diffraction-based imaging methods. He is currently a post-doctoral fellow in the department of Inorganic Chemistry and Catalysis under Professor Bert M. Weckhuysen and Assistant Professor Andrew M. Beale at Utrecht University. His current research focus is the development of X-ray and Raman based imaging with application to studying the behaviour of supported catalyst under preparation and operando conditions.

A detailed list as of October 1st 2010, of the various publicly accessible beamlines from synchrotrons around the world is given in Table 1. The scope then of this tutorial review will focus on the recent applications of SR imaging methods to study real catalytic systems during both their preparation and under reaction conditions.

Although spectroscopic imaging does not require a SR source per se, there are many benefits to be found in using one. Perhaps the most significant is the intense photon flux across the emission spectrum, some 10^1 to 10^{10} times brighter than conventional laboratory X-ray sources (Fig. 1a). In particular, as detailed in Fig. 1b, this enormous photon flux allows for the acquisition of data with both high spatial (<μm) and time (<ms) resolution. Fig. 1b summarizes the typical spatial and time resolution achievable with synchrotron-based imaging methods.

Other properties inherent to SR which are important for imaging purposes includes high collimation, high temporal coherence, beam stability, polarisation and continuous tunability. What follows in this review are a series of case studies which illustrate the tremendous progress in the application of SR spectroscopic and diffraction imaging methods of catalyst materials over the past 20 years. Attention will be given to studies in which data has been acquired in >1 dimension including 2D (x,y scanning and time-resolved x scanning), 3D (tomography and time-resolved x,y scanning), and 4D (time-resolved x,y,z scanning) imaging. The chosen examples serve to illustrate how the entire catalytic process spanning the evolution of the active site/phase, to molecular adsorption, intermediate formation and eventually to catalyst deactivation have been probed on both individual catalyst particles as well as in whole reactor beds. Initially we begin at the far-left of the emission profile (IR region) in Fig. 1a and move towards higher energies whilst at the same time moving towards larger samples—thus demonstrating the sheer scope of applications that such techniques bring. Finally we will assess what is currently possible as of now, and highlight opportunities on the horizon for this exciting field.

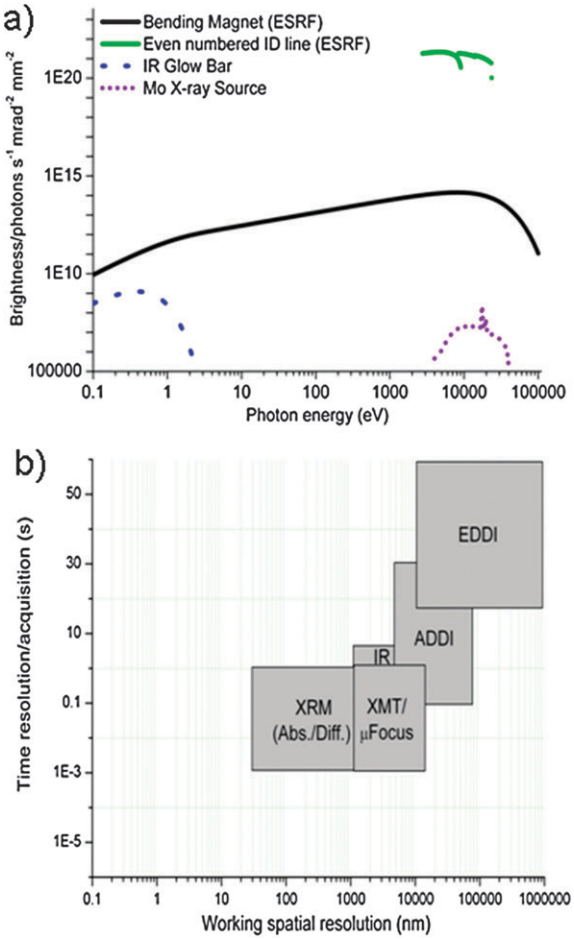

Fig. 1 (a) Typical spectra (brightness against photon energy) comparing an IR glow-bar source, an X-ray tube (40 kV) with a Mo source and synchrotron radiation emitted by a bending magnet and by typical even numbered insertion device lines at the ESRF (6 GeV source, 200 mA current). (b) Spatial and temporal resolution regimes for synchrotron-based techniques. XRM (X-ray Microscopy), XMT (X-ray Micro Tomography), IR (Infra red), ADDI (Angle Dispersive Diffraction Imaging) and EDDI (Energy Dispersive Diffraction Imaging).

Bert M. Weckhuysen

Bert Weckhuysen (42), a native Belgian, received his master degree from Leuven University (Belgium) in 1991. After finishing his PhD studies under the supervision of Prof. R. A. Schoonheydt in 1995, he has worked as a postdoctoral fellow with Prof. I. E. Wachs at Lehigh University (USA) and with Prof. J. H. Lunsford at Texas A&M University (USA). Weckhuysen is since 2000 a full professor in inorganic chemistry and catalysis at Utrecht University. He has authored over 250 publications in peer-reviewed scientific journals and received several research awards, including the 2006 Gold Medal from the Royal Dutch Chemical Society, the 2007 DECHEMA Award from The Max Buchner Research Foundation (Germany) and the 2009 Netherlands Catalysis and Chemistry Award. Weckhuysen is also scientific director of the Dutch Research School for Catalysis (NIOK).

2. Synchrotron IR spectroscopy

The strength of the IR technique is that it can provide information on both the catalyst and the reactants in the gas phase and at the catalyst surface. Since the reactants are normally light(er) elements, the technique is generally better suited for characterising these and therefore it can provide insight into active site-reactant complex formation and the formation of surface intermediates; information that, when contributions from spectators and other non-active components can be decoupled from the data, frequently leads to mechanistic insight into a catalytic reaction. The majority of SR-IR imaging experiments utilise a point source which can be easily collimated and/or focused to diffraction limited spot sizes of *ca.* 5 μm. An additional advantage is that this

Table 1 A list of synchrotron radiation sources, beamlines and imaging techniques available worldwide as of 1st October 2010. Whilst this list is detailed the authors do not claim it to be conclusive. Please see the Electronic Supplementary Information for a version of this Table in which each station has a hypertext link taking the reader directly to the beamline's webpage or else to information concerning the beamline specifications‡

SR Source	*Infra Red Lines*	*X-ray Microscopy Lines*	*X-ray Microprobe Lines*	*X-ray Imaging Lines*
ALBA		MISTRAL (STXM) – Commissioning		
ALS	1.4.3, 1.4.4	6.1.2, 5.3.2 (Polymer Scanning) (STXM)	10.3.1 (μXRF), 10.3.2 (μXAFS), 12.3.2 (μXRD)	2.1, 8.3.2, (Imaging/XMT)
Anka	IR2		Fluo (μXRF), Sul-X (μXAFS./μXRD)	TOPO, IMAGE,
APS			2-ID-B, 2-ID-E (μXRF) 20-BM-B, 13-ID-C,D, 2-ID-D, 20-ID,B,C, 10-ID-B, 18-ID-D (all μXAFS, 18-ID-D μXRD) 26-ID-C, 24-ID-E (Life Sci.), (μXRD, μXRF) 1-ID-C, 24-ID-C/16-ID-B, 34-ID-C, 15-ID-B,C (μXRD)	26-ID-C, 24-ID-E (Life Sci.), 5-BM-C, 10-BM-A,B, 13-BM-D (Imaging/XMT) 32-ID-B,C/7-ID-B,C,D (Phase contrast)
Australian	IR Microspectroscopy		XRF Microprobe	IM beamline (Imaging/XMT/Phase contrast)
BESSY-II	IR-Station		SAMIC-ASAM (μXRF), SMART (μXAFS), XM, mySpot (μXAFS)	XM, BAMline (Imaging/XMT)
BSRF			BL3W1A (μXRF)	
CAMD			XMP (μXAFS)	Tomography
Candle		SXRM		White beam (Proposal Stage)
CHESS			D1 (μXRF)	
CLS	01B1-1 (Mid-IR)	10ID-1 (STXM), 07B2-1	06ID-1 (μXRF)	05B1-1, 05ID-2 (Imaging/XMT)
DAFNE	Sinbad-IR			
Diamond	B22		I06 (μXRD), I18, I20 (EDE) (μXAFS)	I12, I13L, B16 (Imaging/XMT)
ELETTRA	BL9.1		BL3.2L (μXAFS), BL10.1L (μXRF)	
ESRF		ID21	ID01, ID03, ID11 (μXRD), ID13, ID18F, ID24 (EDE) (μXAFS), ID22 (μXRF/μXRD), BM26 (μXAFS), ID26 (μXAFS)	BM5, ID15, ID19 (Imaging/XMT)
Hasylab-DORIS			LHYMO (μXAFS)	BW2, G3, F3 (EDE), HARWI-II (Imaging/ XMT/DEI)
Hasylab-Petra III			P03, P06 (nano/μXAFS, XRD, μSAXS)	P05, P10 (Imaging/XMT)
HSRC		2-17 b		
ISA-Astrid		XRM		
MAX-LAB	(MAX-I) 73			
NSLS	U2A/B, U4IR, U10B	X1A1, X1A2	X13B, X20A, X26A (μXRD), X26/27A & X28B (μXRF)	X2B, (Imaging/XMT), X15A (DEI)
NSRL		U12B		
NSRRC	BL14A1	BL01B1		BL01A1, BL01B1 (Imaging/XMT)
PAL		7B2	IB2 (μXRF), 5C1, 11A (uXRD),	
Photon Factory			BL-4A (μXRF), BL-4B1 (μXRD)	BL-14C1 (Imaging/XMT)
RITS-SR	BL-15	BL-12		
Centre SAGA				BL15 (Imaging)
SLS	X01DB IR	X07DA (STXM)	MicroXAS	X02DA TOMCAT (Imaging/XMT)
Soleil	SMIS		Sextants (μXAFS), Nanoscopium (XAFS, XRD)	Lucia (Imaging) Psiche (Imaging/XMT)
SPring-8	BL43IR	BL24XU	BL37XU (μXRF/μXRD), BL40XU (μXRD)	BL08B2, BL19B2, BL47XU, BL20XU/ BL20B2 (Medical), BL28B2 (EDE) (Imaging/XMT)
SRC	Port 031			
SSLS				PCIT, XDD (Imaging, XMT)
SSRC			SRXFA (μXRF)	
SSRF		BL08U1-A	BL15U1 (μXAFS)	BL10W1 (Imaging)
SSRL		BL6-2A/B/C, 13-1 (STXM)	SSRL2-3, BL6-2A/B/C (μXAFS)	

Acronym list: STXM (Scanning Transmission X-ray Microscopy), XRM (X-ray Microscopy), IR (Infra Red), μXRF/XAFS/XRD (micro-X-ray Fluorescence/X-ray Absorption Spectroscopy/X-ray Diffraction, EDX (Energy Dispersive X-rays), XMT (X-ray micro-tomography) and DEI (Diffraction Enhanced Imaging).

technique is flexible enough so that it can be employed in a number of different measurement formats—*i.e.* transmission, reflectance and (attenuated total) reflection.

To date the application of IR synchrotron radiation for catalytic purposes is somewhat limited. The principle benefits in applying SR-IR is that the improvements in source brightness (*ca.* 50–1000 times) bring about a 2–4 fold improvement in the spatial resolution as well as improvements in the speed of data acquisition;[5] the signal acquisition and data processing equipment being the same IR microscopes/detectors albeit

utilising a much brighter source. In addition the SR-IR source is cold in comparison to the hot glow bar source and shows a more even intensity across the available bandwidth. The following examples illustrate the potential of IR imaging for the characterisation of catalytic materials.

Perhaps the most crucial property that conveys catalytic activity on microporous materials is that of acidity. Acidity arises when Al^{3+}, for example, isomorphously replaces some of the Si^{4+} within the framework, generating an excess charge which is typically balanced by exchangeable cations. The most common of these are protons which act as Brønsted acid sites (Si–O(H)–Al). The bulk distribution of these sites within zeolite crystals can have a significant influence on the catalytic properties of the industrially applied zeolite. Stavitski *et al.* very recently demonstrated the power of SR IR imaging to reveal insight into the strength of these Brønsted acid sites and into the nature and location of the reaction product within polycrystalline H-ZSM-5. In these studies they utilised a 5 by 5 μm beam on station U10B at the NSLS (see Table 1), to study 100 × 20 × 20 μm, coffin-shaped H-ZSM-5 crystals during the oligomerisation of 4-fluorostyrene and 4-chlorostyrene at 373 K as a function of time.[6,7] Initially they utilised SR-IR to profile concurrent changes in monomer consumption and oligomer product formation; a band at 1510 cm^{-1} for the 4-fluorostyrene monomer was observed to decrease in intensity during the reaction whilst a new band at 1534 cm^{-1} appears. Interestingly this 1534 cm^{-1} band shows a strong polarisation dependency. DFT calculations revealed the most likely origin of the 1534 cm^{-1} signal to be the formation of a dimeric carbocation 1,3-bis(4-fluoro/chlorophenyl)-2-buten-1-ylium and that such species when specifically oriented along the length of the straight channels within H-ZSM-5 would exhibit such a polarization dependency. Interestingly H-ZSM-5 crystals comprise a complex intergrown structure, consisting of three subunits rotated by 90° around their common [001] crystallographic axis, resulting in a non-uniform two-dimensional channel network (Fig. 2a). Thus the edges of the crystal contain straight pores which open to the top surface of the crystal and are therefore accessible, whereas the centre region contains straight channels perpendicular to the edges. Hence 2D raster mapping of the 1534 cm^{-1} band (Fig. 2b) with light polarised along the direction of the straight channels in the main body of the crystal, shows a higher signal in the centre than at the edges. These results are very much in line with recent fluorescence and electron microscopy measurements which revealed diffusion barriers between the subunits affecting molecular transport through the crystals.[8]

Like styrenic compounds, thiophenic compounds also lend themselves well to characterisation by IR. Importantly such compounds make up the majority of sulfur species within automotive fuels and one manner in which they can be selectively removed is by selective uptake by zeolites such as H-ZSM-5. With this in mind a second showcase study by the same group, looked at the uptake and distribution of 2-chlorothiophene and its reaction products within large H-ZSM-5 crystals using a combination of SR-IR and Coherent Anti-Stokes Raman Scattering (CARS); the latter technique providing lateral resolution and enabling in addition to confirmative 2D mapping, the 3D imaging of the sample

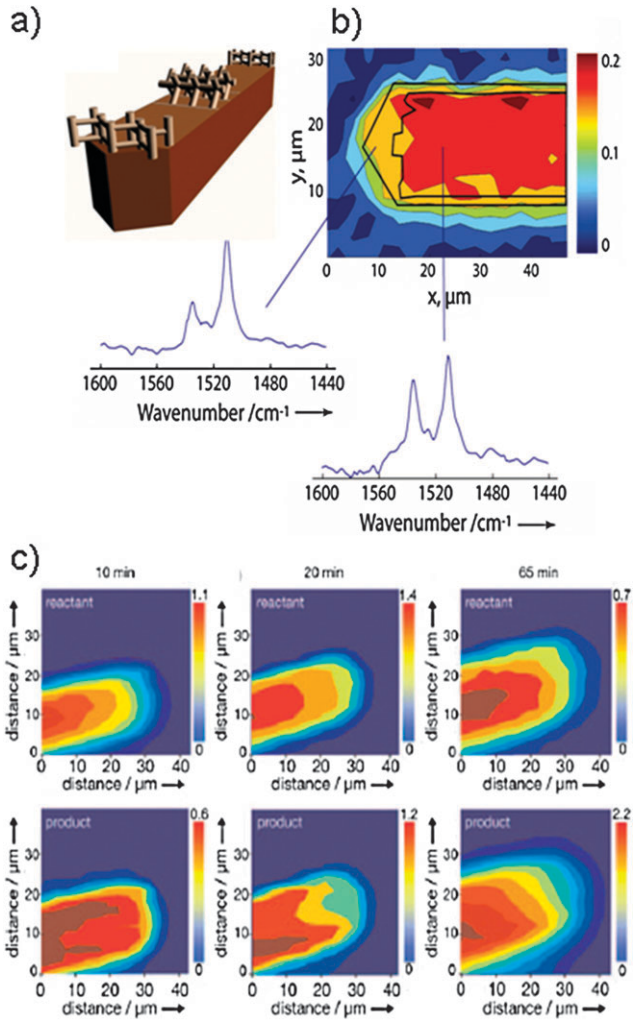

Fig. 2 (a) Zeolite channel alignment in the different regions of the H-ZSM-5 crystal. The zeolite framework, which comprises intersecting straight and zigzag channels, is accessible from the outer surface through openings of the straight pores at the edges and zigzag pores at the body of the crystal. (b) Intensity of the IR band at 1534 cm^{-1} mapped over H-ZSM-5 after reaction. To the left and below the intensity map are example IR spectra taken from the edge and the body of the crystal, demonstrating differences in the intensity ratio of the bands. (c) 2D IR intensity maps of a 2-chlorothiophene/HZSM-5 crystal after 10, 20, and 65 min of reaction for the 1412 cm^{-1} reactant band (top) and 1401 cm^{-1} product band (bottom). The images are presented as temperature maps. (Reproduced with permission from ref. 7 and 9, Copyright Wiley-VCH, 2008 and 2009).

components.[9] As with the styrene oligomerisation study, the authors were able to observe both a gradual decrease in the initial 2-chlorothiophene reactant (C–C stretch @ 1412 cm^{-1}) and the subsequent formation at Brønsted acid sites of oligomer (C–C stretch @ 1401 cm^{-1}) reaction products. The product bands @ 1401 cm^{-1} also showed a strong polarisation dependency thus it was concluded that again there must be elongated molecules entrapped and aligned within the micropores of the zeolite. By focussing on the IR spectral regions that contain information on both the C–C (1350–1550 cm^{-1}) and C–H (2800–3200 cm^{-1}) stretches respectively, the authors were able to identify the most likely form of the oligomer

product(s). Importantly in this work the authors recorded time-resolved 2D IR mapping with a time-resolution of 10 min; sufficiently fast to follow reactant consumption and product formation as a function of 2D space (Fig. 2c). Clearly at the edges of the crystal less reactant and product are present, regardless of the reaction time. Importantly these observations correlated well with the CARS measurements, the cause of which the authors attribute to the intergrowth structure of the crystal and concurrent diffusion barriers.[8]

Although SR based IR studies are currently limited to the above examples there is much scope for a broader application. As has been shown in non SR studies, valuable spatiotemporal information can be obtained from studying processes such as active site evolution, surface coverage, and high throughput catalyst characterisation.[10–12] Furthermore, since the technique is not limited by the physical state of the sample, phenomena such as gaseous/liquid molecular diffusion and reactions in the liquid phase can also be probed in this manner thus rendering the technique very powerful for spatiotemporal imaging. Of particular interest is the increasing availability of the Focal Plane Array (FPA) detector at ultra-bright synchrotron radiation facilities around the world which promises to extend the performance of IR imaging and overcome the existing limitations.[13] For a more detailed evaluation of IR imaging in its current and future state the reader is referred to the review of Stavitski and Weckhuysen in this themed issue.[14]

3. X-Ray imaging

X-Rays have been widely employed for catalyst characterisation, ranging from the study of individual catalyst particles to the profiling of reactors on stream. The highly penetrating nature of X-rays or their 'high mean-free path' means that it is possible to interrogate samples in a number of different ways (see Table 1) to obtain for example elemental composition, local atomic coordination/oxidation state, crystallinity, density, *etc*., often under real reaction conditions with a sufficient time resolution to reveal chemical and structural change. As with IR, depending on the energy range used, it is also possible to probe both bulk and surface species, although there is less spectral information available at the softer edges, being essentially limited to X-ray Absorption Near Edge Spectroscopy (XANES). A spatial resolution as low as a few 10's of nm is now achievable for some techniques from 3rd and 4th generation SR sources—thus bringing the realisation of single particle imaging closer to reality.[15,16]

The manner by which an X-ray image can be obtained for a sample is essentially defined by the beam form, the sample-detector geometry and the nature of the measurement; for a more comprehensive overview of the common acquisition methods the interested reader is referred to the reviews of Bertsch and Hunter as well as Bonse and Busch.[17,18] For catalyst characterisation purposes three general beam types have been used; confocal (microscopy) beam, letter-box beam and pencil beam. Three types of measurement have also been performed using both mono and polychromatic beams; transmission (absorption contrast), fluorescence and diffraction (image contrast) radiography and tomography. It is interesting to note that pencil beam techniques ('lenseless imaging') offers perhaps the best potential for very high (<10 nm) spatial resolution although for practical reasons to date the best resolution (*ca*. 30 nm) within realistic measurement times has been obtained in X-ray confocal microscopy mode.[19,20] A particular advantage of X-ray imaging is that it is often possible to simultaneously collect more than one signal *i.e*. transmission and fluorescence, transmitted and scattered beam in order to obtain additional complementary and highly congruent information on the sample for cross-correlative analysis.

3.1 Soft X-ray transmission microscopy (STXM) for imaging catalytic solids at the nanoscale

Fischer–Tropsch synthesis (FTS) utilises synthesis gas (a mixture of CO and H_2) to produce hydrocarbons and thus offers a potential alternative to natural fuel reserves for transportation fuel. The Fe_2O_3 supported on SiO_2 catalysts represent perhaps the most economical and environmentally friendly type of FT catalyst for gas-to-liquid (GTL), coal-to-liquid (CTL) and biomass-to-liquid (BTL) conversion and has recently been studied using STXM in order to follow key phase changes and the evolution and location of carbon species during both pre-reduction and the FTS reaction itself.[21,22] The technique uses soft X-rays (between 100–2000 eV) and as such probes the 1s core (K-edges) electrons of light elements or the 2p core ($L_{2,3}$ edges) of heavier elements. The monochromatic X-ray beam is focused by a Fresnel zone plate lens to *ca*. 30 nm spot-size. The sample is then raster-scanned (1–5 ms per pixel/ with a typical image containing 20 × 20 pixels) with synchronized detection of transmitted X-rays to generate images (Fig. 3a). *Chemical* imaging and XANES spectra are obtained using image sequence (stack) scans over a range of photon energies (typically spanning 25 eV/edge). Total acquisition times per edge are in the order of 30–60 min. For more detailed information about the technique the reader is referred to the recent review by de Groot *et al*.[23] The crux of the technique is that it provides information on valence state and specific bonding environments of the probed elements in a non destructive manner—hence offering unprecedented insight at the nanoscale into the behaviour of this catalyst. However due to the soft nature, signal attenuation is a problem (the penetration distance in air being only 0.4–4 mm) thus the sample thickness cannot be greater than 20 μm. Therefore a specially designed nanoreactor comprising two 10 nm thick SiN_x windows was constructed which allowed for the obtaining of data under reaction conditions (typically 1.2 bar and up to 773 K). The reactor is then mounted onto a piezoelectric stage with nanometre precision, thus allowing for the recording of STXM images with a 35 × 35 nm step size. 2D images were created using the C K edge (284.2 eV), O K edge (543.1 eV), and Fe L_2 and L_3 edges (706.8 eV and 719.9 eV, respectively) to distinguish between the various species present in the sample and to identify at the nanometre scale, the relationship between the various elemental components. Fig. 3(b)i contains a 2D image of the starting phase in which the plot is dominated by the contributions from α-Fe_2O_3 (orange) and SiO_2 (white)—the SiO_2 contribution being determined

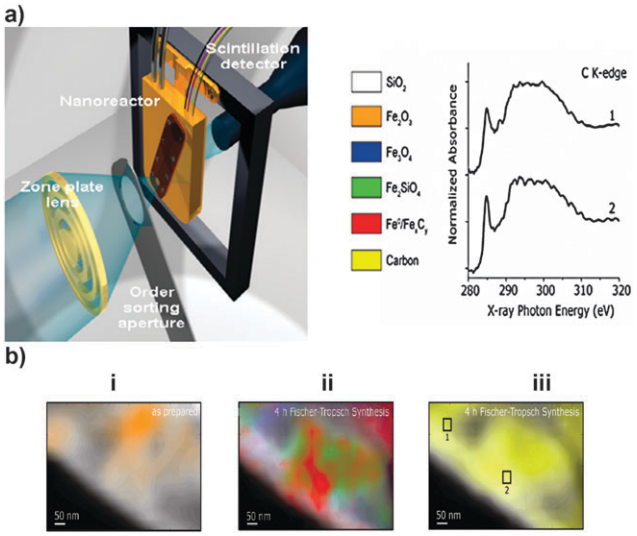

Fig. 3 (a) Setup of a STXM microscope, with from left to right, the zone plate lens, order sorting aperture, the nanoreactor and the scintillation detector. In (b) are given example C K-edge XANES spectra recorded at two given points in (a) which contain nanoscale X-ray images which detail the stages that iron (initially as Fe_2O_3 supported on SiO_2), (i) evolves (ii/iii) as the Fischer–Tropsch reaction proceeds. Boxes 1 and 2 in (iii) correspond to the C K-edge spectra shown in Fig. 3(a). (Adapted with permission from ref. 23, Copyright Wiley-VCH, 2010).

indirectly by a linear-combination fitting of the oxygen K edge data. After 2 h of 'activation' in H_2 at 350 °C, the catalyst material undergoes significant yet spatially uneven compositional change; α-Fe_2O_3 transforms into a mixture of Fe_3O_4, Fe_2SiO_4, and FeO. During FTS reaction, the majority of the Fe_3O_4 phase was revealed to undergo further conversion to metallic Fe (20%) and Fe_2SiO_4 (75%) respectively. Interestingly analysis of the C K edge shows that C is co-located in Fe-rich regions and furthermore that the corresponding C K-edge spectra are consistent with the presence of sp^2 hybridized species, typical of FeC type phases whereas in Fe poor regions, the spectra are more consistent with the presence sp^3-like FTS reaction products. The presence of reactant carbon species in iron-deficient areas indicates that the support might have some role in the spillover of (hydro)carbon species from the metal to the support, thereby preventing blocking of the active sites of the catalyst.

A quite elegant example that demonstrates the importance of coupling nano-resolution with that of the chemical insight that can be obtained was recently published by Zhou *et al.* where STXM was used to chemically image RuO_2 nano-layer coated multi-walled carbon nanotubes (termed hereafter RuO_2/MWCNT).[24] These materials have already shown much promise for a number of applications and it was proposed that the interaction between catalyst and the support (*via* defects) is crucial in affecting the materials' physical properties—thus nano-scale resolution coupled with a typical energy resolution of 0.05 eV is required for such characterisation purposes. Shown in Fig. 4 are the resultant chemical maps for (b) RuO_2, (c) the MWCNTs, and (d) oxidized MWCNTs. These conventional 2D elemental maps demonstrate that the impregnation of RuO_2 on the MWCNTs results in an inhomogeneous sample: O K-edge measurements revealing that RuO_2 is not uniformly coated on the tubes whereas in contrast, the terminal O groups cover nearly the whole surface of the MWCNT. The C K-edge measurements however show that the graphitic framework of the MWCNTs remains intact upon coating with RuO_2 thus preserving the electrical conductivity of the sample. By analysing the C K-edge XANES spectra the authors observed a 0.3 eV red shift for the π^* transition and a reduction in its intensity which infers direct evidence of charge transfer from RuO_2 to the C 2p-derived π^* states at the MWCNTs interface. This conclusion was confirmed by concurrent evidence of O p-electron depletion seen in the O K-edge. Interestingly the presence of an additional feature at 289.3 eV, indicates that the C environment is more strongly oxidized than a C atom in the CO_2H functional group; the interaction of RuO_2 with MWCNTs appears to be therefore a chemically strong bond. Such insight is vital for both the design of functional materials and the understanding of their chemical properties and suggests that techniques such as STXM will play a very important role.

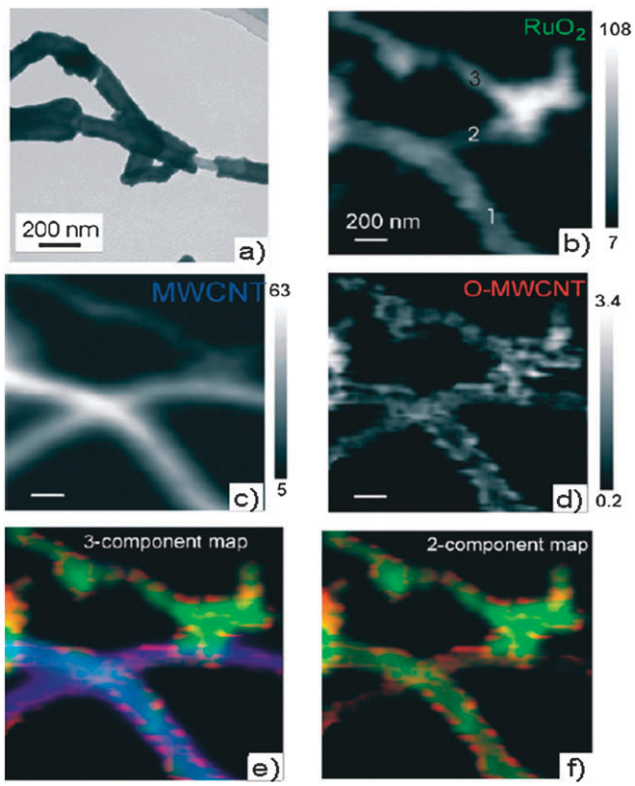

Fig. 4 (a) TEM and (b)–(f) STXM chemical maps of RuO_2/MWCNTs: (b) RuO_2 and (c) MWCNTs, grey scale represents the thickness in nm; (d) surface oxygen-containing functional groups on MWCNTs, the grey scale is proportional to the extent of surface oxidation (1 prior to RuO_2 coating, intensity greater than 1 shows the effect of oxidation); (e), (f) colour composite maps for three or two components (green: RuO_2, blue: MWCNT, red: O-containing groups on MWCNTs). The component maps are rescaled individually between 0 and 255 in each colour channel. (Reproduced from ref. 24 by permission of the Royal Society of Chemistry).

3.2 Hard X-ray microprobes for imaging zeolite single crystals

Hard X-ray microscopy (where $E > 2$ keV) offers comparable spatial resolution to STXM although to date there has been no reported study where complementary XANES data has also been obtained with this spatial resolution. The majority of studies therefore utilise X-ray microprobes which, whilst being unable to provide such high resolution are able to provide more detailed chemical information since harder X-rays allow for probing of the continuum states (μXAFS). In a recent study by Kox *et al.* microfocus X-ray fluorescence spectroscopy focused by Fresnel zone plates to a beam size of 0.21×0.8 μm^2 was used to study the interaction and distribution of thiophenic compounds within the pores of large ($100 \times 20 \times 20$ μm) H-ZSM-5 crystals @ 493 K.[25] The setup employs a scanning double crystal monochromator thus full X-ray fluorescence (XANES) spectra were collected at each pixel of the Ge detector in order to obtain structural and chemical insight into the nature of the framework-thiophene interaction. Fluorescence maps of the various components from an individual zeolite H-ZSM-5 crystal are shown in Fig. 5 and reveal an even distribution of the framework components (Si/Al) and thiophenic compound(s). Despite being unable to determine precisely a structure of the thiophene-Brønsted acid site complex, DFT modelling of the XANES data at least did suggest that the S atom was in close proximity (*ca.* 2.5 Å) to a framework O atom. UV-Vis and confocal fluorescence microscopy was then used to identify the presence of two types of thiophenic species within the zeolite crystal; dimeric carbocations (by virtue of a band at 410 nm in the UV-Vis data) and polymeric carbocations (590 nm) aligned along the straight channels in the body of the crystal. Hence the presence of at least two different species within the crystal might well explain why it had not been possible to determine the nature of the S 'environment' within the zeolite. Interestingly polymeric thiophenic species were only present within the zeolite crystal and not on a physical mix of silica/boehmite and was indicative of the importance of zeolite Brønsted acid sites for the catalytic decomposition of thiophenic compounds.

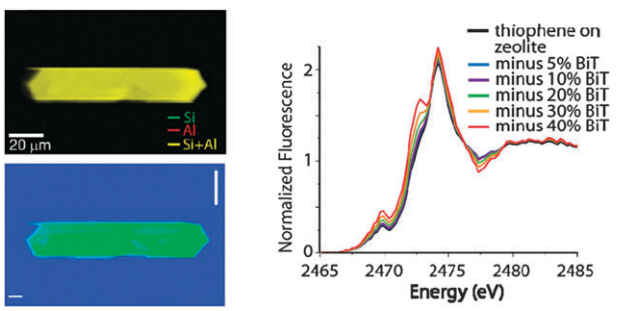

Fig. 5 Top left, 2-D X-ray fluorescence map of an individual H-ZSM-5 zeolite crystal indicating the location of Si (green) and Al (red) atoms and bottom, the concentration of adsorbed sulfur (thiophene) after 10 s. On the right are shown the sulfur K-edge spectra of the zeolite H-ZSM-5 crystal after reaction with thiophene at 493 K. For comparison, the influence of the presence of increasing amounts of bithiophene on the fit has also been included. (Reproduced with permission from ref. 25, Copyright Wiley-VCH, 2010).

3.3 X-Ray absorption tomography for the characterisation of catalytically produced polyolefin particles

85–95 million tons of polyolefins (essentially homopolymers and copolymers of propylene and ethylene) are produced around the world annually. Most industrial catalysts for olefin polymerization are heterogeneous Ziegler–Natta ($Ti/MgCl_2$) or CrO_x supported on SiO_2/TiO_2 systems. It has been proposed that during polymer synthesis, the supported catalyst fragments become embedded within the evolving polymer particles; sometimes the fragments are distributed towards the particle periphery whilst at other times (dependent on the catalyst and polymerisation conditions) they form random distributions.[26] This latter observation was made in some of the very first synchrotron X-ray microtomography studies on such particles. Measurements were carried out using the NSLS X26 X-ray microscopy facility which utilises a collimated source beam (4 μm^2) and scintillation detector that is used to measure the attenuation of the X-ray beam through the specimen. The tomogram is then obtained using a first generation computed tomography (CT) data collection technique involving the performing of multiple transmission measurements across the material before the sample is rotated through a small angle (*ca.* 0.1°) and multiple scans are repeated until a minimum angle of 180° is covered. The tomogram is then reconstructed using standard reconstruction algorithms. Ferrero *et al.* used this technique to explore particles taken directly from the polymerization reactor (propylene was polymerized in a slurry process over $Ti/MgCl_2$ at 50 °C and 0.1 MPa) and were characterised in terms of fragment size distribution, fragment location and void morphology within a single particle.[27] Analysis of the tomograms revealed the formation of a catalyst/polymer particle composite with fairly uniform embedded catalyst fragments (estimated to be 5% of the total volume) and that no correlation could be found between the size of the fragments or their radial distribution within the overall individual particle. In addition the polymer distribution appeared highly heterogeneous; some high density polymer regions up to 50 μm in size were observed in addition to pores of the size-order of 10–40 μm representing some 50% void space. Furthermore, the polymer itself looked like it consisted of 'agglomerates' of surprisingly uniform subparticles rather than growth of a single particle.

As previously illustrated, microtomography studies can provide detailed insight into the micromorphology of polymer particles. Such studies yield important structural insight such as the extent of internal porosity which influences polymerisation efficiency and physical strength. For example a recent study by Boden *et al.* examined the influence of polymerisation conditions (particularly the H_2 partial pressure) on the growth and structure of nascent polyolefin particles.[28] Important internal differences in the relative amounts of what were termed 'less porous fused morphologies', 'highly porous clustered morphologies' and 'embedded large voids' could be seen between the two particles. At lower H_2 partial pressures (1 bar), a smaller particle with less voids and larger amounts of less porous fused morphologies results. In addition, the voids were less well distributed than when a higher partial pressure (2 bar) was used to form an altogether larger particle, thus

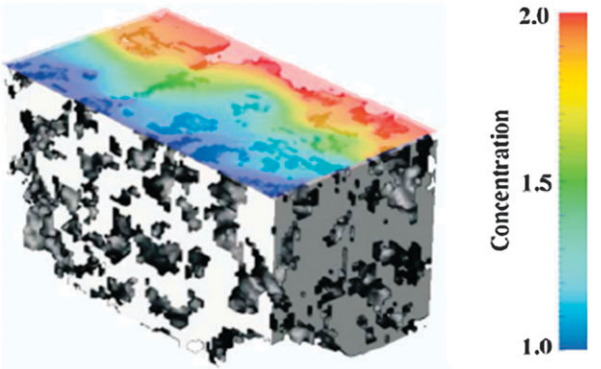

Fig. 6 Monomer concentration profile inside a reconstructed polyethylene particle. The arbitrary concentration difference is set between two opposite walls. (Reproduced with permission from ref. 29, Copyright Wiley-VCH, 2008).

particles prepared under a low gas partial pressure are mechanically stronger than those formed under high partial pressures. In a second recent study, Seda *et al*. utilised 3D tomograms as a starting point for performing computer simulations to study diffusion within real porous polyolefin particles.[29] Although the simulations performed considered only Fickian diffusion, interesting insight into the influence of particle structure on: (i) stationary diffusion, (ii) dynamics of degassing, and (iii) combined polymerization reaction and diffusion in fully-grown polyolefin particles could be obtained. For example, the studies demonstrated that the concentration of monomer (ethylene and propylene) was shown to be susceptible to mass transport limitations in the polymer phase, affecting the rate of polymerization (or composition and sequence lengths in copolymers) (see Fig. 6). Whilst this study nicely illustrated the benefits of performing such XMT measurements, the authors themselves alluded to an important limitation of these simulations; namely that since they were using a lab-based instrument, the spatial resolution was limited to 10 μm. This meant that they could not consider the role that smaller pores/closed-off openings could play in diffusion processes. We observe that this would be much less of an issue at synchrotron sources, where much smaller spot sizes can be routinely achieved and thus may represent the way forward for future studies.

3.4 Hard X-ray absorption tomography of an iron-based Fischer–Tropsch catalyst

Promoters are often added to FT catalysts like Fe_2O_3 supported on SiO_2, in order to optimise their performance (both in terms of activity and selectivity). The concentration and distribution of these species within the active particle can have important implications for the catalytic activity. In a recent XMT study by Jones *et al*. the group analysed the samples taken from a constant-stirred-tank-reactor (CSTR) used for FT synthesis.[30,31] Test samples were periodically withdrawn from the reactor for characterization and quenched by quick cooling to room temperature in an inert atmosphere to avoid any oxidation. Tomography data were recorded on these samples in transmission (absorption) and fluorescence modes (μXRF) using bending magnet beam lines (X26A and X27A) of the NSLS (see Table 1) using an X-ray energy of 14 keV. Thus it was possible to map various metal concentrations over the surface of the samples. The fluorescence (XRF) maps of Fe, Ni, Cu, Zn, and Pb, as observed for one sample analysed, are shown in Fig. 7. The colour scales show the relative concentrations in each pixel after normalization to the NSLS X-ray ring current. The maps showed that there were appreciable differences in the Fe concentrations in the FT wax on this size scale. Perhaps of more interest was the presence of so many additional components in the catalyst, accounting for *ca*. 10% of the total mass. The correlations between different elements indicate that Ni, Cu, Zn, and Pb/As are not always associated with the Fe in the catalyst material; it was not clear whether these additional components were part of the initial formulation or else had been deposited on the catalyst during reaction. Either way it is highly likely that such species influence the catalyst activity and product distribution during the FT reaction. Fluorescence CMT measurements on the same sample revealed sections of Fe inhomogeneity with localized regions of higher concentrations (yellow colored voxels) in accordance with the XRF results. Void spaces created during the sample preparation were also observed and are seen as the blue colored voxels. Corresponding CMT maps for the other elements could not be obtained since their concentrations were too low to obtain a reliable signal. It is clear that a more detailed study is warranted in order to understand the origin of the additional components as well as their significance in influencing catalyst performance. Furthermore, a study as a function of time in the reactor may yield important insight into long term modes of deactivation.

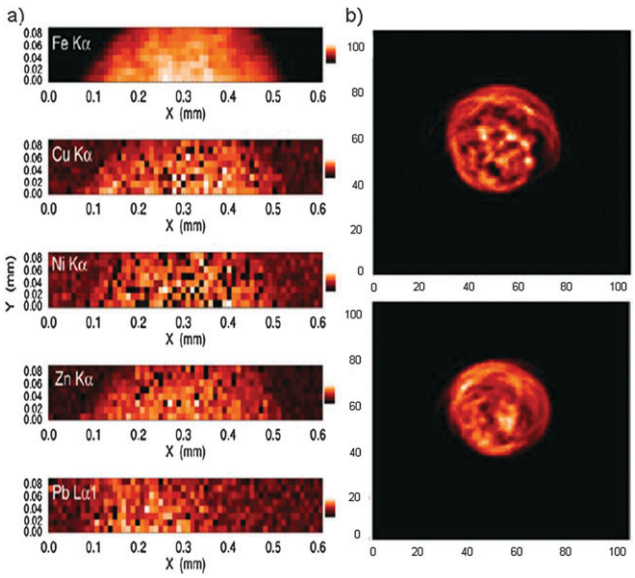

Fig. 7 (a) Maps of Fe, Ni, Cu, Zn, and Pb metals detected in a sample taken during the FT reaction. The maps show the variability of concentration on a pixel-to-pixel size scale. (b) Fe distributions in two fluorescence tomographic sections through the FT waxy sample show variability of the catalyst concentrations. The pixel size for the images is 0.010 mm × 0.010 mm. (Reproduced with permission from ref. 31, Copyright Springer Science, 2005).

3.5 Imaging of the water formation process in fuel cells

Low temperature polymer electrolyte membrane (PEM) fuel cells are one of the most promising candidates for future mobile and stationary applications. In PEM fuel cells, hydrogen and oxygen react to form water and electrical energy. Protons migrate through the membrane and recombine with oxygen on the surface of the cathodic catalyst where oxygen is reduced and forms water. Crucial then to the optimal operation is the rapid removal of water from the catalyst surface and the adjacent porous gas diffusion layer (GDL). Water accumulation can both hinder the transport of reactant and product gases as well as limit the maximum achievable power density. In order to optimise fuel cell operation, it is necessary to first obtain insight into the process of liquid water formation and transport. Although neutron radiography is very useful for studying such processes the resolution is poor (optimally this is around 20–50 μm although typically remains 100–250 μm) and the neutron flux is comparatively low. In a recent study by Manke *et al.* XMT was employed with a spatial resolution of 3 μm and a time resolution of 5 s (1 s acquisition and 4 s detector readout) was used to gain a realistic image of the transport and production of liquid water.[32] Experiments were performed at the BAMline at the Synchrotron BESSY in Berlin, Germany. The experiment was performed at 13 keV since this energy represent a suitable trade-off between obtaining sufficient transmission yet sensitivity to the imaging of water. A 2048 × 2048 pixel camera setup (Princeton VersArray 2048B with a Gadox scintillator screen) was used to capture image area sizes up to 7 × 7 mm with pixel sizes between 1.5 and 3.5 μm with a physical spatial resolution of typically 3–8 μm. Imaging was performed on a single cell setup and measurements were performed through an 8 mm hole (sealed) in the metal end-plates and focussed on the 1 mm wide flow-field channels within the blank graphite composite plates (SGL Carbon). A typical raw image as obtained during the experiment is shown in Fig. 8 showing the flow field channels on the cathode and anode side. The white spots in the image are water clusters. Impressively the water droplets are displayed with such a high accuracy that even details like the droplets' contact angle and orientation in space can be determined.

The amount of liquid water produced in the cell strongly depends on the electric output current density and the fraction of total gas input which is consumed in the cell at the electrodes. The water distributions for two different operating conditions are displayed in Fig. 8 together with the corresponding enlargements of the areas marked in red. The water thickness was quantified by means of the attenuation coefficient of water at the used X-ray energies. Under dry conditions only small water clusters of about 10–20 μm in diameter were visible within the GDL pores indicating that most water is in the gas phase. Under wet conditions many water clusters appear up to 300 μm in diameter, containing up to several hundred or thousand picolitres of water. The mode of water transport varies between different locations in the cell. The authors observed an 'eruptive transport mechanism' (many droplets of liquid water in the gas diffusion layers are ejected) at some spots whilst at others a continuous flow was

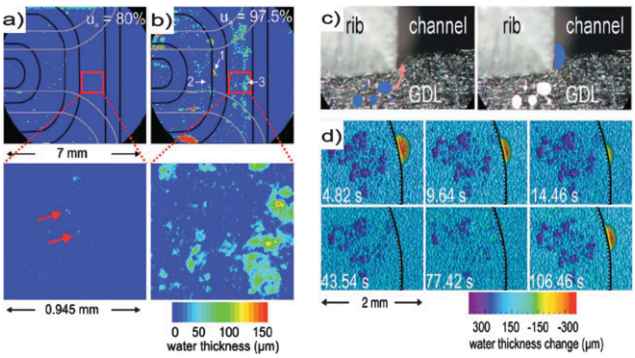

Fig. 8 (a) and (b) Normalized radiographs of the operating fuel cell displaying the water distribution for two different operating conditions ('dry' (a) and 'wet' (b)) with corresponding enlargements of the areas marked in red in the second row. Flow field channels are marked by dark lines. Red arrows point to examples of water clusters whereas the white arrows labeled 1, 2 and 3 refer to points where water formation was profiled in the study. (c) and (d) demonstrate the process of eruptive water ejection from the gas diffusion layer GDL to the cathodic flow field channel. In (d) water (blue) inside the pores of the cathodic GDL is ejected into the flow field channel. Dark blue and purple areas represent reduced amounts of water in the GDL pores while other colors indicate an increased water level. Within this time the pores are emptied and the water moves into the channel where it forms a droplet at the wall side. After some time the water droplet evaporates and the pores are filled again *i.e.*, the blue areas disappear until a new ejection takes place. (Reproduced with permission from ref. 32, Copyright American Institute of Physics, 2007).

observed. After about 100 s the pores are filled again up to a certain level before the next eruption occurs (Fig. 8d). The behaviour is periodic with an almost constant frequency, lasting for the duration of the experiment (45 min) and always takes place in approximately the same pores of the GDL—due to inhomogeneities in the GDL fibre network.[33] In conclusion, synchrotron X-ray radiography proved to be an invaluable tool for *in situ* investigations of operating fuel cells, yielding insights into water evolution, water transport processes, and multiphase effects. Such insight was very much in agreement with previously proposed theoretical models and with recent findings during fluorescent imaging studies.

3.6 Real-time analysis of a Rh/Al_2O_3 packed-bed plug-flow reactor

The use of Rh/Al_2O_3 as the catalyst for methane partial oxidation is regarded as one of the most promising technologies for hydrogen production in plants of medium size. The modus operandi of the catalyst is however not known, although it was proposed from previous studies that the nature of the catalyst changes along the length of the bed. Hence, 2D-mapping of this catalyst during reaction was performed at HASYLAB station X1 by Grunwaldt *et al.* in order to gain insight into the reaction mechanism.[34] For this study a 2.5% Rh/Al_2O_3 catalyst was fixed between two glass wool plugs in a 1.5 mm thick capillary (*ca.* 10 mm bed length). A letter-box beam 1 mm × 0.5 mm (length × height) and CCD (charged coupled device)-area detector was used for mapping the axial coordinate of the catalyst bed. The X-ray energy was scanned in the XANES region around the Rh K-edge in steps of one eV

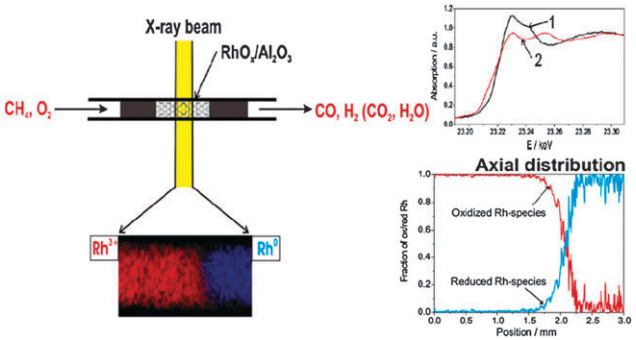

Fig. 9 Schematic of measurement setup and distribution of oxidized Rh-species (*i.e.*, Rh^{3+}, red) and reduced Rh-species (*i.e.*, Rh^0, blue) in the cell as derived from the XANES spectra top right (spectra 1 (oxidised) black line and spectra 2 (reduced) red). The axial distribution (bottom right) is taken from the middle of the fixed-bed reactor. (Adapted with permission from ref. 34, Copyright 2006 American Chemical Society).

(from 23 190 to 23 375 eV). The exposure time for each image was 30 s. The resultant images are derived per pixel as a function of the intensity I (E, x, y) or I_0 (E, x, y) for images taken with or without sample, respectively. The integral of the absorption is then calculated for each pixel and energy is then obtained so that for any given pixel in these images, a full absorption spectrum is available. Additional least squares fitting of these spectra was used to produce quantitative 2D-maps of the Rh-oxidation state distribution in the catalytic reactor.

Fig. 9 depicts the experimental setup and 2D X-ray transmission image of the reactor during the partial oxidation of methane at 283 °C (6 h) and in particular to study the ignition process of partial methane oxidation over supported Rh-particles. From the Rh K-edge XANES data it is possible to distinguish between Rh in its oxidized (3+) or reduced state (0) from features in the XANES. In this case, the X-ray absorption is higher on the left-hand side of the reactor, near the gas inlet than on the right-hand side. Interestingly a sharp (*ca.* 100–200 μm) diagonal gradient of reduced Rh species is seen at the interface which remains stable (with catalyst performance) for several hours. The observed profile further indicates that methane combustion at low temperature dominates in the first part of the reactor, whereas methane reforming occurs in the second part. In subsequent studies, Hannemann *et al.* and Grunwaldt *et al.* showed that the position of the Rh^{3+}/Rh^0 front is a function of the space velocity and the reaction temperature; both an increase in space velocity and temperature results in the Rh^{3+}/Rh^0 front moved towards the inlet.[35–37] The observation in the mass spectrometry trace of products due to combustion and reforming is also consistent with the formation of Rh^0 species in the downstream part of the reactor.

Since the catalytic system and reaction processes are well known, the observations made using XANES imaging could be understood in terms of the observed activity measured using the mass spectrometer product trace. However, for unknown reaction systems it might be that such *a priori* knowledge is not available and as such, XANES imaging alone might not be suitable to provide such clear insight. For example it is difficult to rule out the presence of Rh(I) species in this sample using XANES alone. Having access to the additional information that could be provided by EXAFS imaging for example would enable for a more comprehensive analysis of this reaction system.

3.7 2D cross-sectional imaging of a CuO/ZnO containing packed bed reactor

The previous study utilised a letterbox beam for the full-field 2D imaging of a reactor bed, however the approach does not provide sufficient depth resolution so as to be able to observe variation from within the packed bed reactor. Such depth information allows for evaluating whether bed by-passing is a problem and to ensure that the reactor is working under plug-flow conditions. For this, CMT scans in the hard X-ray range are required and were employed on BM5 of the ESRF and 1-ID of the APS (see Table 1) to study a 30% CuO/ZnO Water Gas Shift-type catalysts undergoing redox cycling in 4% H_2/He and 2% O_2/He at 200–300 °C gas mixtures.[38,39] CMT scans were performed whereby a full XANES spectra was collected at each location in a virtual section (x, y) through the catalyst bed. The method was implemented by combining a quick scanning monochromator and data acquisition system with a scanning pencil beam microprobe (although in theory it is also possible to collect data in the sub-μm range) setup based on parabolic refractive X-ray lenses. An absorption spectroscopy tomogram is then recorded at each position r and rotation ϕ by scanning the sample through the microbeam using several translational and rotational movements and recording an absorption spectrum (projection). In this work, XANES spectra were acquired within 1 s although the use of an oscillating monochromator means that it is possible to acquire data in as little as 10 ms.[40] Data can be acquired in either fluorescence or transmission mode although in the former case, the signal is strongly attenuated.

A reconstructed 2D slice through the catalyst bed at 8995 eV is given in Fig. 10 and to illustrate the chemical information available, XANES spectra from 2 pixels (grey arrows) in the reconstructed 2D image are also shown. Whilst the 2D slice revealed density differences across the sample, analysis of the XANES spectra by linear combination fitting using reference spectra of Cu^0, Cu_2O and CuO, revealed differences in copper compounds present. This compositional analysis is then reconstructed over the 2D slice resulting in a series of images pertaining to the amounts of Cu(I) and Cu(0) respectively. These results demonstrate clearly what is possible with such a technique particularly if, as the authors propose, the energy range of the monochromator could be adjusted to cover the full EXAFS regime. This would provide more chemical information and broaden the applicability of the technique towards tackling more complex systems.

3.8 Imaging of a single catalyst extrudate during preparation

For maximum performance, catalytically active components are normally dispersed within/supported on various types of inorganic structures whose shape and size is typically determined by the end application. There are at least five different types of catalyst 'body': extrudates, pellets, monoliths, foams

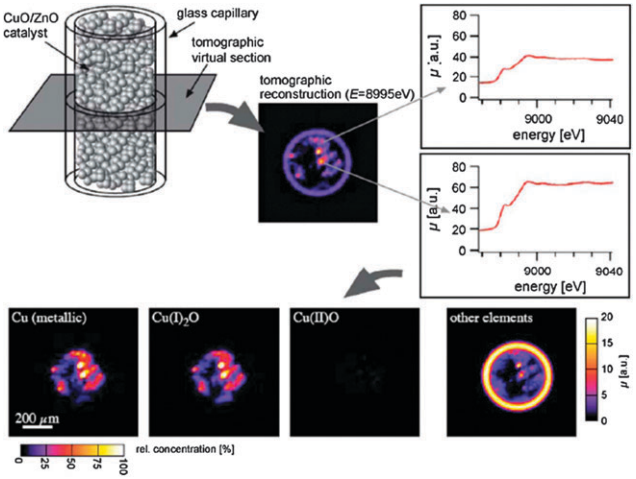

Fig. 10 Scanning microtomography combined with X-ray absorption spectroscopy at the Cu K-edge. In a virtual slice of a capillary (here the catalyst bed contains Cu/ZnO particles in BN) the X-ray absorption of the sample as function of energy is measured by scanning the sample in translation (90 steps of 10 μm each) and rotation (101 steps over 360 s), acquiring at each position a full absorption spectrum (see grey arrows). The absorption coefficient can be reconstructed for each energy at each location on the virtual slice. Thus, in each location on the reconstructed slice a full XANES (in principle it could also be possible to obtain EXAFS data although to date this has yet to be reported) spectrum is obtained. From these data the concentration of the different Cu-species can be extracted by fitting a linear combination of reference spectra to the spectrum at each location on the virtual slice. (Reproduced with permission from ref. 39, Copyright American Institute of Physics, 2003).

and spheres. The main advantage of using such bodies is that, in comparison to fine powders, the pressure difference across the catalyst bed is reduced. Crucial to the functioning of these catalyst 'bodies' is the preparation method in which the active component and catalyst body are brought together. The efficiency of the final catalytic system depends on both the nature and distribution of the active phase thus the preparation process is essential, with the final distribution of the active component over the porous support being governed by a combination of physical and chemical processes.[41] Recently X-ray imaging methods such as XMT have been used to obtain a better understanding of these processes. Some notable examples include the determination of the active washcoat thickness on hierarchic metallic hollow sphere structures and the distribution of the zeolitic component in fluid catalytic cracking (fcc) catalysts.[42] Similar, although non-SR XMT, studies of note include a study of wetting of alumina spheres and two separate studies into the crystallisation of ZSM-5 and Pd-Ag/SiO_2 xerogels on alumina foams.[43–45] However, one subject in particular has received a lot of attention lately: the imaging of transition metal containing catalyst extrudates.

Transition metal oxides anchored to a support are widely used as heterogeneous catalysts in a number of important industrial chemical processes. Their activity is brought about by the formation of unique metal–support interactions, which typically results in materials containing highly dispersed metal/metal oxide species stabilized in a particular electronic and/or coordination state. In recent times both spectroscopic and scattering techniques have been developed to obtain spatial information on the distribution of chemical species within catalyst bodies.[46] These tools provide 'non-invasive', spatially resolved insight into the influence of the preparation procedure and the effect that reaction conditions have on the active phase distribution. This information can be used to better understand the preparation and deactivation steps in order to develop better catalyst materials. To date, X-ray techniques such as SXMT and Tomographic Energy Dispersive Diffraction Imaging (TEDDI) have been utilised to probe the active component distribution in both 2D and 3D.[31,47] More recently these studies have been extended to provide time-resolved 2D information on both the impregnation and calcination/activation processes.

Perhaps the most well-studied catalyst bodies are the hydrotreating catalysts. These consist of either Ni-Mo/γ-Al_2O_3 or Co-Mo/γ-Al_2O_3 impregnated on either cylindrical or tri-lobal bodies and have been studied both by XMT (for pre and post reaction characterisation) and TEDDI (impregnation and calcination). The pre and post-characterisation study of NiMo/γ-Al_2O_3 by Jones *et al.* represents perhaps one of the pioneering studies utilizing XMT for the characterization of catalyst bodies.[48] The technique was used to produce 2D elemental maps of the elements comprising a catalyst with a spatial resolution around *ca.* 5–10 μm. Elemental maps were produced *via* XMT both through the measurement of the linear attenuation coefficients and by detection of the fluorescent X-rays; the presence of a scanning monochromator also enabling, if required, the acquisition of XANES data. Elemental contrast images of the pellets before and after reaction are shown in Fig. 11. The darker areas seen in the used catalyst correspond to large concentrations of Mo, suggestive of sintering/re-distribution during reaction. Furthermore, the maps showed that the pellet appears to swell with reaction time. Since the concentration of Mo in the pellet was high it was also feasible to obtain a specific Mo distribution map over the sample by measuring above and below the Mo K-edge (in a sort of phase contrast tomography experiment) with the resultant 'difference map' shown in Fig. 11c suggesting that Mo was evenly distributed over the sample. Such a measurement approach has also proved useful in revealing the internal structure of such samples as well as inhomogeneities during preparation/immobilization of Cu and Pd on alumina pellets, and hence is applicable across the entire catalyst lifecycle.[35,49]

Absorption radiography and tomography are already well-established techniques, although are somewhat limited to providing elemental distribution maps. Thus the technique does not provide the chemical information necessary (*i.e.* whether it is amorphous or crystalline, oxidic or metallic) to develop the all important structure–function relationships required to understand catalytic processes. However, the recently developed TEDDI technique can do this and as such offers great potential for characterising catalysts.

Beale *et al.* demonstrated TEDDI to profile supported Mo/γ-Al_2O_3 and Co-Mo/γ-Al_2O_3 catalysts.[47] A schematic of the experimental setup from station 16.4 of the now redundant Daresbury synchrotron radiation source (SRS) used in these measurements, is given in Fig. 12a. The scanned volume

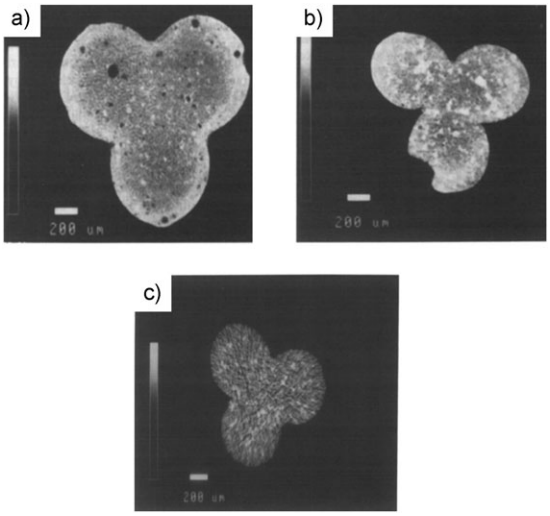

Fig. 11 Linear attenuation coefficient tomograms of Ni-Mo hydrotreating pellets before (a) and after reaction (b). Note the change in size and morphology resulting from use. The pixel size employed was 5 μm with a slice thickness of 10 μm. (c) contains a tomogram of the Mo concentrations obtained from subtraction of the signal above and below Mo absorption K-edge tomograms. (Reproduced with permission from ref. 31, Copyright Springer Science, 2005).

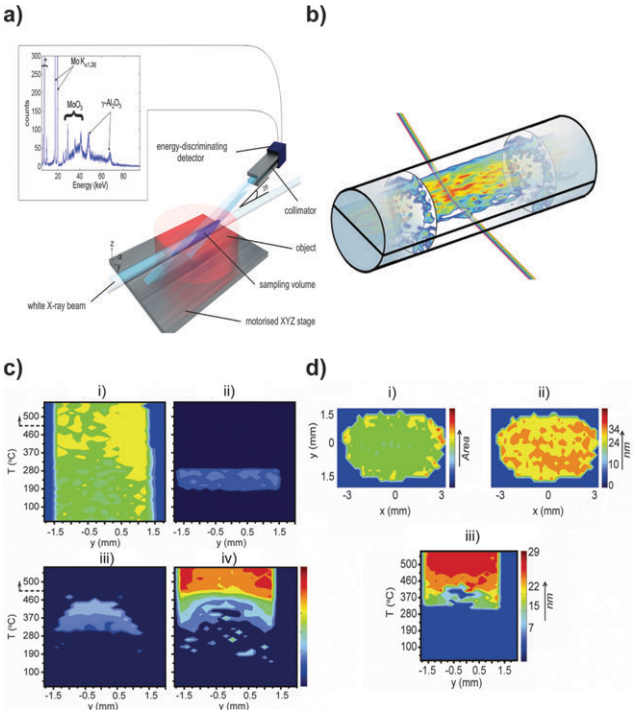

Fig. 12 (a) Schematic of the TEDDI measurement setup. (b) Reconstructed 3D image using absorption path length correction algorithm combining the data obtained from two different 2D scans (termed *y*, *z* and *x*, *y*) on a Co-Mo/γ-Al_2O_3 catalyst illustrating the presence of 'hot spots' (*i.e.* concentration build-up).[55] (c) contains *y* scan data as a function of T for (i) Ni fluorescence at 7.5 keV ($Ni_{K\alpha}$); (ii) the diffraction peak at 36.9 keV (unknown Ni-containing crystalline phase), (iii) the 50.2 keV (101) reflection of Ni_3C; and (iv) the 57.6 keV (200) reflection of metallic fcc Ni, all in the $[Ni(en)(H_2O)_4]Cl_2$/γ-Al_2O_3 pellet. In (d) are shown *x*, *y* maps detailing (i) metallic Ni distribution in the $[Ni(en)(H_2O)_4]Cl_2$/γ-Al_2O_3 pellet after calcination at 500 °C, (ii) particle size distribution of metallic Ni in the same slice of the pellet after calcination at 500 °C, and (iii) evolution of metallic Ni crystallites as a function of the *y* direction of the catalyst body. (Adapted with permission from ref. 50, copyright 2009 American Chemical Society).

element is defined by the intersection of the incident X-ray beam (for these experiments $x\ y\ z = 0.1 \times 0.1 \times 0.1$ mm), which corresponds to the various spatial resolution(s) of the experiment) with the diffracted beam that passes through the post-sample collimator into the detector. Many such volume element locations can be visited by intelligently scanning the sample through the X-ray beam and collecting the X-ray signal from each location by means of an energy-dispersive Ge detector. The advantage with this technique is that the same detector records the signal for both the diffraction pattern and fluorescence peaks from the defined volume element (*ca.* 15 s/volume element); therefore, a full scan gives rise to a complete diffraction and fluorescence record of the whole sample region of interest (2D imaging in the space of a few hours). Provided then at least one unique 'diagnostic' diffraction peak can be identified for each phase, TEDDI offers a means of obtaining concentration maps for individual crystalline phases within a catalyst body in a time and space resolved manner.

Fig. 12a shows a typical detector signal for a Mo/γ-Al_2O_3 catalyst body (1.5 mm ϕ × 10 mm) after calcination. A number of peaks can be identified in this pattern, which are either due to fluorescence (*ca.* 17.4 (Mo $K_{\alpha1,2}$) and 19.6 keV ($Mo_{K\beta}$)) or diffraction (reflections at 67 and 78 keV by the γ-Al_2O_3 phase and at 25, 27 and 29 keV corresponding to the (101), (400/201) and (210) reflections from MoO_3). The distribution of these signals (Z-Y), obtained from peak profiling from both techniques point to the formation of an egg-shell distribution of MoO_3.[31,47] Importantly, in hydrotreatment catalytic testing this sample showed low activity; most likely due to the difficulty in forming the active MoS_2 nanoslabs from large MoO_3 crystallites. It was proposed that the 'egg-shell' effect might be caused by either an insufficient equilibration time during the impregnation step or due to the high concentration of molybdenum exceeding the dispersion limit of the support.

Perhaps more interestingly the authors performed additional 2D cross-sectional scans in the *x*, *y* and *z*, *x* planes, thus providing phase distribution information along the length of the extrudate. This is illustrated as an amalgamated image in Fig. 12b, which contains a series of measurements performed in the *x*, *y* plane for the calcined Co-Mo/γ-Al_2O_3 catalyst body. Although there were no 'detectable' amounts of crystalline Co or Mo containing phases present, X-ray fluorescence information revealed various signal 'hot spots' (red coloured) along the long axis of the body. Particularly at the extremes of the body and more generally from the centre of the *x*, *y* scan. The signal at the extremes are almost certainly due to a larger contact area with the impregnation solution, although it is currently much more difficult to explain the 'hot-spots' observed in parts of the middle. Since they are not due to any density differences, they most likely reflect variation within the

structure caused by the extrusion process, which may have an important influence on impregnation.

Through the development of an environmental cell with temperature and gas control, mounted on a movable (x y z) stage, the application of this technique was extended to the performing of time-resolved 2D TEDDI measurements on a larger catalyst extrudate sample (3.0 mm ϕ × 3.0 mm l).[50] Since the sample size was now twice as large, the authors used a larger beam (x y z = 2.47 × 0.1 × 0.2 mm) and larger step sizes (Δy = 0.2 mm) in order to obtain a 2D cross-section within a reasonable time resolution (*ca.* 4 h). The setup was used to study the evolution of two Ni/γ-Al_2O_3 hydrogenation catalyst bodies prepared from two different precursor complexes: $[Ni(en)_3](NO_3)_2$ and $[Ni(en)(H_2O)_4]Cl_2$ during calcination. The study reveals that both samples yielded an fcc Ni/γ-Al_2O_3 catalyst material, yet the decomposition pathways for the two complexes were different. As Fig. 12c reveals, for the $[Ni(en)_3](NO_3)_2$ sample, the initial crystalline phase $Ni(en)_3(NO_3)$ directly decomposes to yield an even distribution of crystalline fcc Ni nanoparticles (Debye-Scherrer analysis of the 220 reflection suggesting an average size of the order of 5 nm).[50] Whereas the $[Ni(en)(H_2O)_4]Cl_2$/γ-Al_2O_3 sample undergoes a number of changes in order to form the final fcc Ni phase. Whilst this sample contains no Ni-containing crystalline phase, Ni fluorescence maps reveal the Ni to be evenly distributed in the form of the complex $[Ni(en)(H_2O)_4]Cl_2$/γ-Al_2O_3. The precursor then decomposes in a stepwise manner, forming a variety of crystalline phases including an unknown phase, followed by Ni_3C and finally crystalline fcc Ni. 2D y z mapping reveals significant differences in the phase composition across the sample: 40% of the total Ni content at the core of the pellet exists as Ni_3C, whereas at the edges this phase comprises no more than 20%, the reminder being fcc Ni. At 460 °C only fcc Ni is observed although the average particle size is in this case much larger 24–34 nm (Fig. 12d) when compared to that produced using $Ni(en)(NO_3)_2$, although the precise mechanism by which these large metallic Ni particles form is not clear. Whilst this study could not provide mechanistic insight into the phase evolution process, it was able to reveal that the formation of an active component is a multi-step evolutionary process and that this process shows significant spatial variation. Improving the acquisition time and data quality may well be necessary in order to obtain such chemical insight. In this regard TEDDI experiments utilising energy dispersive 2D pixelated array detectors or high energy monochromatic diffraction imaging (TADDI) hold much promise here.[51–55]

4. Recent, current and future developments in the field and where these might lead to

The examples described above clearly illustrate the wide applicability of imaging methods and the benefits of using such methods to more fully characterise catalytic samples and processes. However, in many respects the examples represent only a fraction of what is possible with SR in this regard. Here we discuss future research possibilities in terms of both methods and materials.

4.1 Broadening the scope of scanning X-ray microscopy

The coupling of high spatial resolution with the chemical sensitivity of STXM renders it a powerful technique for imaging catalytic materials. One can imagine that future developments in zone plate technology will result in improvements in this resolution, with spot sizes expected to break into the single figures of nm. However STXM suffers from two major drawbacks; by being limited to the collection of XANES data, the chemical information extractable is limited and furthermore X-ray absorption by the sample limits the conditions under which the samples can be studied. From a technical viewpoint then the development of Hard X-ray TXM (nanoscopy) with a resolution that matches or betters STXM would represent a significant breakthrough in this field provided suitable zone plates can be constructed. The issue of recording EXAFS data is however another matter since by stepping through the energy range the focal length of the zone plates changes and one has to accurately match this with a corresponding change in same position through the bandwidth, which is technically challenging. Thus it might be that lenseless pencil-beam based techniques from 4th generation SR sources are a more viable option for such purposes. In an ideal world one would like to be able to have simultaneous access to both hard and soft X-ray energies so as to be able to image the catalyst and adsorbents at the catalyst surface. Thus what is required is a highly tunable setup which could prove to be very powerful in studying for example catalyst poisoning processes, spillover effects, metal–support interactions in heterogeneous solids to name but a few. Ultimately a combination of high resolution and tunability might enable for *in situ* monitoring of a catalyst 'single site'. Whether such developments in X-ray microscopy can be realised within reasonable timescales remains to be seen.

Another recent technique development comprising a novel coupling of scanning probe microscopy and X-ray absorption spectroscopy may yet offer a viable alternative. The setup utilises a tapered optical fiber tip of a scanning near-field optical microscope (SNOM) to detect the X-ray excited optical luminescence (XEOL) from a sample irradiated with an SR beam.[56,57] A shear-force feedback is employed both to regulate the probe–sample distance and to record the topographical image of the surface. The absolute positioning of the tip and of the sample with respect to the X-ray microbeam is then performed using a six-independent-axis system. In order to collect the XEOL signal using the optical fiber tip, the imaging is carried out scanning the sample under the probe, which is kept fixed with respect to the radiation beam. The setup has recently been installed at the ESRF on beamline ID03 and integrated with the beamline software control and data acquisition system. With such a setup a lateral resolution of about 100–200 nm and vertical resolution of 3 nm has been possible and has to date been used to study pure ZnO and mixed $ZnWO_4$–ZnO nanostructured thin films, obtaining atomic maps of both Zn and W distributions (Fig. 13). In addition, it is also possible to record high quality XANES spectra for chemical imaging purposes thus with improved lateral resolution, this technique combination could rival/complement TXM as the ideal nano-imaging technique for characterising catalyst solids.

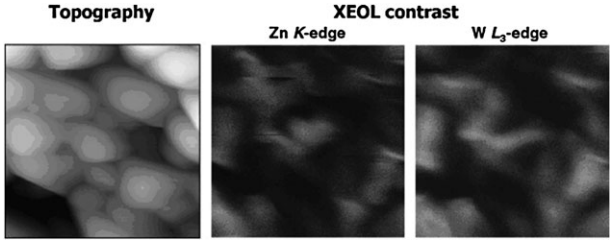

Fig. 13 Topography (left) and XEOL contrasts at the Zn K (centre) and W L_3-absorption edge (right) of a $ZnWO_4$/ZnO thin film. Image size 18 × 18 μm. The XEOL contrast image corresponds to the difference between two XEOL images measured above and below the correspondent absorption edge. (Reproduced with permission from ref. 56, Copyright Elsevier, 2009).

4.2 Diffraction imaging

Since the properties of many heterogeneous catalysts rely on the atomic ordering of active sites for their properties, diffraction remains the primary technique for their study. Thus far we have shown the power of TEDDI yet the time/data/space resolution is insufficient to be able to image changes at the submicron scale. Very high energy monochromatic beams from an ID line can in this regard possess many advantages over their white beam counterparts. Data collection times are typically sub-second, beam spot sizes are smaller (down to *ca.* <50 μm) and enable for better spatial resolution and the data is inherently better in quality so as to enable for more detailed characterisation (*i.e.* Rietveld refinement). Furthermore when an additional energy dispersive detector is used, parasitic signals such as fluorescence and Compton can also be collected to yield complementary information, as has been demonstrated recently.[53,58,59] However it should be noted that such studies are best served by using very high energy (>60 keV).[60]

Of particular interest has been the recent development of the diffraction equivalent of STXM, known as scanning X-ray diffraction microscopy (SXDM) where the pixel size is as small as 18 nm. Initial experiments were performed in which 201-by-201 diffraction patterns (300-nm spot size) were collected, each pattern being collected for only 50 ms—this fast collection time being possible in no small part due to the use of the recently developed fast single-photon counting Pilatus detector with no read-out noise.[20] It is predicted that a combination of higher coherent flux and improved focusing optics should soon provide conditions for better-than-10-nm resolution. Should this be possible it might prove very powerful in examining particle size and phase heterogeneity in supported catalysts and for example, to allow for the identification of crystalline domains in zeolite precursors.[61,62] With sufficient data quality so as to be able to perform Rietveld analysis, it would be possible to examine not only simple phase distributions, but also to examine their interaction of these phases with the catalyst support—thought to be a crucial parameter in determining why some catalysts are more active than others despite possessing the same composition.[63]

4.3 Simultaneous imaging; when two birds in the bush can be worth more than one in the hand

Technique combining is already well established for measurements in 0D and the benefits of such an approach have been well documented.[64–66] From an imaging perspective only a handful of examples exist where combined, congruent simultaneous information has been obtained from the same sample. These examples really only represent the tip of the iceberg of what is possible when combining measurements. We delineate the subject matter at this point into two sections; the collection of multiple signals from the same incident radiation source and simultaneous measurement with non-X-ray techniques.

Measurements in which multiple signals are collected from the same source beam are straightforward. Such a setup normally measures two different signals in the same detector (*i.e.* the fluorescence and diffraction signals in TEDDI) or else utilises a separate detector for each technique (XRF and XMT). In the former case it is often simply a case of deconvoluting the two contributions. If we consider from an imaging perspective what has not yet been done but yet could well be possible, one immediately thinks of a combination involving a high energy monochromatic beam and 2D detector covering a sufficiently large d-range to acquire simultaneous SAXS and WAXS signals and even Pair Distribution Function (PDF)/SAXS/WAXS in either a radiographic or tomographic format, although this is probably best carried out using two detectors. By utilising a photodiode as a beamstop it would also be possible to collect XMT data thus allowing for the simultaneous acquisition of XMT/SAXS/WAXS data.[53,67,68] An additional advantage of such setups is that the signal comes from the same spot in the sample. We note that in comparison, technique combinations in which two separate detectors have been employed are more common; as testament to this a number of publications already exist on this subject matter.[31,48,54,69]

Somewhat more interestingly are the recent endeavours to develop synchrotron beamlines in which two separate beams can be focussed on the same part of the sample at the same time. This allows for example for simultaneous imaging with a combination of fixed monochromator/scanning monochromator setup for combined diffraction/XAFS scanning.[70] Alternatively and as has been recently proposed, a portion of the storage ring beam could be taken off at two points of a bending magnet to yield both IR and X-ray radiation which, if the associated technical challenges could be overcome, could be focussed to the same part of the sample, resulting in a very powerful technique combination for catalyst imaging purposes.[71,72] Following on from the last example are the combinations of X-rays with non-X-ray based techniques which normally requires the insertion of additional apparatus into the beamline. Whilst this is an already established field, from an imaging perspective it is only recently that such setups have been designed and commissioned.[66] These include the coupling of a micro Raman probe head to the end station on ID13 @ ESRF which delivers a focussed laser spot (*ca.* 1 m in diameter) to the same position on the sample as the X-ray beam (for μXRD).[73] The microprobe is coupled to the beamline control software for automatic triggering during X-ray data collection and therefore the two techniques can be used to simultaneously map an area of the sample. Another technique combination of note is the *in situ* atomic force microscopy (AFM)/microfocussed scanning X-ray diffraction

microscopy (μSXDM) setup developed on ID01 @ ESRF.[74] The combination allows an alignment of the sample with respect to the AFM tip and the incident X-ray beam to a very high accuracy and is thus a powerful technique for imaging amongst other things, well-dispersed nanoparticles located on a sample grid.

Finally it is worth considering two recent developments in source technology and the influence these could have on future imaging studies. Namely the Free Electron Laser (FEL) and table-top synchrotrons. Whilst FELs are not per se new, they have been, much like 1st generation synchrotron facilities, the preserve of the high energy physicist. However as with early SR facilities, recent developments such as the soft X-ray FLASH facility in Germany and the recently commissioned Linac Coherent Light Source at SLAC have been designed with the end-user in mind.[75,76] With some further expected developments, FELs are now poised to take centre stage as the premier source of tunable, intense, coherent photons of either ultra-short time resolution or ultra-fine spectral resolution, from the far infrared to the hard X-ray regime (a wavelength of 0.1 nm is currently being targeted for the European XFEL project).[75] FELs can provide an unprecedented enhancement anywhere from 10^6–10^{11} in the peak brightness when compared to a SR storage ring. This is expected to herald a new age of discovery since the ultra-short pulses will yield both femto second time resolution and meV spectral resolution which can be used to explore the temporal evolution of phenomena such as atomic motion, phase transitions and chemical reactions in real time in diverse fields such as biology, chemistry and material science (single-particle imaging).

Despite the major advantages of SR light, the development of new laboratory X-ray sources continues. Recent developments have concentrated on making light sources which are small enough to fit into a laboratory yet possess fluxes that are comparable to those of a 3rd generation source. Examples include high intensity microfocus X-ray sources with dramatically higher flux and ultrashort duration pulses thereby enabling dynamic measurements and the highly versatile and commercially available tabletop synchrotrons which have already been successfully employed for amongst other things, phase contrast and projection XMT, XAFS, XRF analysis and IR absorption spectroscopy.[77–79] The expected developments here in both source brilliance and detector sensitivity may well eventually allow for SR imaging in the home laboratory.

4.4 Brightness: a cautionary note

Crucial to the obtaining of data with better spatial or chemical resolution is the availability of a spectral profile with greater brightness. Yet this brings its own problems. In particular beam effects such as thermal load, photoionisation and photoreactivity need to be taken into consideration especially since highly focussed beams deliver greater power densities. This may well limit the application of very bright sources for time-resolved imaging purposes in that sacrificial trade-offs might need to be made between the spatial, time and chemical resolution possible in an experiment, especially so if more than one analytical beam is focussed on the sample at the same spot. However this is by no means a new problem and there already exist a number of possibilities to tackle such issues. For example, the radiation dose for the sample can be controlled by either continuous movement of the beam or else by controlling the exposure by shuttering, whereas for some measurements a judicious choice of wavelength or edge energy (*i.e.* K *vs.* L_3) allows for the suppression of specific modes of sample degradation.[60,80] Thus whilst this means that certain samples may prove to be unsuitable for such high resolution studies, it should not be considered as an unmanageable problem.

5. Conclusions

The current development of new SR sources and new beamlines continues apace and as such nowadays there exists a great many opportunities for imaging of catalytic solids with high spatial resolution and chemical sensitivity. Whilst such techniques will not always be able to provide all of the answers to a chemical problem, the fact that such methods can be readily employed under *in situ*/operando conditions makes them highly suitable for revealing new and valuable insights, thus rendering such techniques as key components in the catalyst scientist's toolbox.

Acknowledgements

The authors would like to thank NWO for a Veni (AMB) and Vici (BMW) grant respectively. Both EPSRC and ESRF are gratefully acknowledged for access to the respective measurement facilities. We would also like to thank a couple of the contributors to some of the research featured in this review article (Prof. Paul Barnes and Dr Matthew G. O'Brien) for both their insight and technical know how. The reviewers are also thanked for the useful and insightful comments made.

References

1 B. M. Weckhuysen, *Angew. Chem., Int. Ed.*, 2009, **48**, 4910–4943.
2 A. Urakawa and A. Baiker, *Top. Catal.*, 2009, **52**, 1312–1322.
3 J. E. Daniels and M. Drakopoulos, *J. Synchrotron Radiat.*, 2009, **16**, 463–468.
4 P. Kraft, A. Bergamaschi, C. Broennimann, R. Dinapoli, E. F. Eikenberry, B. Henrich, I. Johnson, A. Mozzanica, C. M. Schleputz, P. R. Willmott and B. Schmitt, *J. Synchrotron Radiat.*, 2009, **16**, 368–375.
5 W. D. Duncan and G. P. Williams, *Appl. Opt.*, 1983, **22**, 2914–2923.
6 E. Stavitski, E. Pidko, M. Kox, E. Hensen, R. van Santen and B. Weckhuysen, *Chem.–Eur. J.*, 2010, **16**, 9340–9348.
7 E. Stavitski, M. H. F. Kox, I. Swart, F. M. F. de Groot and B. M. Weckhuysen, *Angew. Chem., Int. Ed.*, 2008, **47**, 3543–3547.
8 L. Karwacki, M. H. F. Kox, D. A. M. de Winter, M. R. Drury, J. D. Meeldijk, E. Stavitski, W. Schmidt, M. Mertens, P. Cubillas, N. John, A. Chan, N. Kahn, S. R. Bare, M. Anderson, J. Kornatowski and B. M. Weckhuysen, *Nat. Mater.*, 2009, **8**, 959–965.
9 M. H. F. Kox, K. F. Domke, J. P. R. Day, G. Rago, E. Stavitski, M. Bonn and B. M. Weckhuysen, *Angew. Chem., Int. Ed.*, 2009, **48**, 8990–8994.
10 R. B. Biniwale, H. Yamashiro and M. Ichikawa, *Catal. Lett.*, 2005, **102**, 23–31.
11 F. Qin and E. E. Wolf, *Ind. Eng. Chem. Res.*, 1995, **34**, 2923–2930.
12 A. Urakawa, N. Maeda and A. Baiker, *Angew. Chem., Int. Ed.*, 2008, **47**, 9256–9259.

13 C. Petibois, G. Deleris, M. Piccinini, M. Cestelli-Guidi and A. Marcelli, *Nat. Photonics*, 2009, **3**, 179–179.
14 E. Stavitski and B. M. Weckhuysen, *Chem. Soc. Rev.*, 2010, **39**, DOI: 10.1039/c0cs00064g (this themed issue).
15 A. Schropp, P. Boye, J. M. Feldkamp, R. Hoppe, J. Patommel, D. Samberg, S. Stephan, K. Giewekemeyer, R. N. Wilke, T. Salditt, J. Gulden, A. P. Mancuso, I. A. Vartanyants, E. Weckert, S. Schoder, M. Burghammer and C. G. Schroer, *Appl. Phys. Lett.*, 2010, **96**, 091102.
16 T. R. Neu, B. Manz, F. Volke, J. J. Dynes, A. P. Hitchcock and J. R. Lawrence, *FEMS Microbiol. Ecol.*, 2010, **72**, 1–21.
17 P. M. Bertsch and D. B. Hunter, *Chem. Rev.*, 2001, **101**, 1809–1842.
18 U. Bonse and F. Busch, *Prog. Biophys. Mol. Biol.*, 1996, **65**, 133–169.
19 J. M. Rodenburg, A. C. Hurst, A. G. Cullis, B. R. Dobson, F. Pfeiffer, O. Bunk, C. David, K. Jefimovs and I. Johnson, *Phys. Rev. Lett.*, 2007, **98**, 034801.
20 P. Thibault, M. Dierolf, A. Menzel, O. Bunk, C. David and F. Pfeiffer, *Science*, 2008, **321**, 379–382.
21 E. de Smit, I. Swart, J. F. Creemer, C. Karunakaran, D. Bertwistle, H. W. Zandbergen, F. M. F. de Groot and B. M. Weckhuysen, *Angew. Chem., Int. Ed.*, 2009, **48**, 3632–3636.
22 E. de Smit, I. Swart, J. F. Creemer, G. H. Hoveling, M. K. Gilles, T. Tyliszczak, P. J. Kooyman, H. W. Zandbergen, C. Morin, B. M. Weckhuysen and F. M. F. de Groot, *Nature*, 2008, **456**, 222–225.
23 F. M. F. de Groot, E. de Smit, M. M. van Schooneveld, L. R. Aramburo and B. M. Weckhuysen, *ChemPhysChem*, 2010, **11**, 951–962.
24 J. G. Zhou, J. Wang, H. T. Fang, C. X. Wu, J. N. Cutler and T. K. Sham, *Chem. Commun.*, 2010, **46**, 2778–2780.
25 M. H. F. Kox, A. Mijovilovich, J. Sattler, E. Stavitski and B. M. Weckhuysen, *ChemCatChem*, 2010, **2**, 564–571.
26 K. W. Jones, P. Spanne, W. B. Lindquist, W. C. Conner and M. Ferrero, *Nucl. Instrum. Methods Phys. Res., Sect. B*, 1992, **68**, 105–110.
27 M. A. Ferrero, R. Sommer, P. Spanne, K. W. Jones and W. C. Conner, *J. Polym. Sci., Part A: Polym. Chem.*, 1993, **31**, 2507–2512.
28 S. Boden, M. Bieberle, G. Weickert and U. Hampel, *Powder Technol.*, 2008, **188**, 81–88.
29 L. Seda, A. Zubov, M. Bobak, J. Kosek and A. Kantzas, *Macromol. React. Eng.*, 2008, **2**, 495–512.
30 K. W. Jones, H. Feng, A. Lanzirotti and D. Mahajan, *Nucl. Instrum. Methods Phys. Res., Sect. B*, 2005, **241**, 331–334.
31 K. W. Jones, H. Feng, A. Lanzirotti and D. Mahajan, *Top. Catal.*, 2005, **32**, 263–272.
32 I. Manke, C. Hartnig, M. Grunerbel, W. Lehnert, N. Kardjilov, A. Haibel, A. Hilger, J. Banhart and H. Riesemeier, *Appl. Phys. Lett.*, 2007, **90**, 174105.
33 I. Manke, C. Hartnig, N. Kardjilov, H. Riesemeier, J. Goebbels, R. Kuhn, P. Kruger and J. Banhart, *Fuel Cells*, 2010, **10**, 26–34.
34 J. D. Grunwaldt, S. Hannemann, C. G. Schroer and A. Baiker, *J. Phys. Chem. B*, 2006, **110**, 8674–8680.
35 J. D. Grunwaldt, B. Kimmerle, A. Baiker, P. Boye, C. G. Schroer, P. Glatzel, C. N. Borca and F. Beckmann, *Catal. Today*, 2009, **145**, 267–278.
36 B. Kimmerle, J. D. Grunwaldt, A. Baiker, P. Glatzel, P. Boye, S. Stephan and C. G. Schroer, *J. Phys. Chem. C*, 2009, **113**, 3037–3040.
37 S. Hannemann, J. D. Grunwaldt, N. van Vegten, A. Baiker, P. Boye and C. G. Schroer, *Catal. Today*, 2007, **126**, 54–63.
38 C. G. Schroer, M. Kuhlmann, T. F. Gunzler, B. Lengeler, M. Richwin, B. Griesebock, D. Lutzenkirchen-Hecht, R. Frahm, A. Mashayekhi, D. R. Haeffner, E. Ziegler, J. D. Grunwaldt and A. Baiker, *Phys. Scr.*, 2005, **T115**, 1026–1028.
39 C. G. Schroer, M. Kuhlmann, T. F. Gunzler, B. Lengeler, M. Richwin, B. Griesebock, D. Lutzenkirchen-Hecht, R. Frahm, E. Ziegler, A. Mashayekhi, D. R. Haeffner, J. D. Grunwaldt and A. Baiker, *Appl. Phys. Lett.*, 2003, **82**, 3360–3362.
40 M. Richwin, R. Zaeper, D. Lutzenkirchen-Hecht and R. Frahm, *Rev. Sci. Instrum.*, 2002, **73**, 1668–1670.
41 A. V. Neimark, L. I. Kheifez and V. B. Fenelonov, *Ind. Eng. Chem. Prod. Res. Dev.*, 1981, **20**, 439–450.
42 W. Kaltner, K. Lorenz, B. Schillinger, A. Jentys and J. A. Lercher, *Catal. Lett.*, 2010, **134**, 24–30.
43 W. van der Merwe, W. Nicol and F. de Beer, *S. Afr. J. Sci.*, 2006, **102**, 585–588.
44 F. Scheffler, R. Herrmann, W. Schwieger and M. Scheffler, *Microporous Mesoporous Mater.*, 2004, **67**, 53–59.
45 C. Alie, F. Ferauche, A. Leonard, S. Lambert, N. Tcherkassova, B. Heinrichs, M. Crine, P. Marchot, E. Loukine and J. P. Pirard, *Chem. Eng. J.*, 2006, **117**, 13–22.
46 L. Espinosa-Alonso, A. M. Beale and B. M. Weckhuysen, *Acc. Chem. Res.*, 2010, **43**, 1279–1288.
47 A. M. Beale, S. D. M. Jacques, J. A. Bergwerff, P. Barnes and B. M. Weckhuysen, *Angew. Chem., Int. Ed.*, 2007, **46**, 8832–8835.
48 K. W. Jones, P. Spanne, S. W. Webb, W. C. Conner, R. A. Beyerlein, W. J. Reagan and F. M. Dautzenberg, *Nucl. Instrum. Methods Phys. Res., Sect. B*, 1991, **56–57**, 427–432.
49 L. Ruffino, R. Mann, R. Oldman, E. H. Stitt, E. Boller, P. Cloetens, M. DiMichiel and J. Merino, *Can. J. Chem. Eng.*, 2005, **83**, 132–139.
50 L. Espinosa-Alonso, M. G. O'Brien, S. D. M. Jacques, A. M. Beale, K. P. de Jong, P. Barnes and B. M. Weckhuysen, *J. Am. Chem. Soc.*, 2009, **131**, 16932–16938.
51 R. J. Cernik, K. H. Khor and C. Hansson, *J. R. Soc. Interface*, 2008, **5**, 477–481.
52 V. Middelkoop, P. Boldrin, M. Peel, T. Buslaps, P. Barnes, J. A. Darr and S. D. M. Jacques, *Chem. Mater.*, 2009, **21**, 2430–2435.
53 P. Bleuet, E. Welcomme, E. Dooryhee, J. Susini, J. L. Hodeau and P. Walter, *Nat. Mater.*, 2008, **7**, 468–472.
54 P. Bleuet, L. Lemelle, R. Tucoulou, P. Gergaud, G. Delette, P. Cloetens, J. Susini and A. Simionovici, *TrAC, Trends Anal. Chem.*, 2010, **29**, 518–527.
55 O. Lazzari, S. Jacques, T. Sochi and P. Barnes, *Analyst*, 2009, **134**, 1802–1807.
56 S. Larcheri, F. Rocca, D. Pailharey, F. Jandard, R. Graziola, A. Kuzmin, R. Kalendarev and J. Purans, *Micron*, 2009, **40**, 61–65.
57 S. Larcheri, F. Rocca, F. Jandard, D. Pailharey, R. Graziola, A. Kuzmin and J. Purans, *Rev. Sci. Instrum.*, 2008, **79**, 013702.
58 M. G. O'Brien, A. M. Beale, S. D. M. Jacques, T. Buslaps, V. Honkimaki and B. M. Weckhuysen, *J. Phys. Chem. C*, 2009, **113**, 4890–4897.
59 M. G. O'Brien, A. M. Beale, S. D. M. Jacques, M. Di Michiel and B. M. Weckhuysen, *ChemCatChem*, 2009, **1**, 99–102.
60 M. G. O'Brien, A. M. Beale, S. D. M. Jacques, M. Di Michiel and B. M. Weckhuysen, *Appl. Catal., A*, 2010, DOI: 10.1016/j.apcata.2010.06.027.
61 H. Karaca, J. P. Hong, P. Fongarland, P. Roussel, A. Griboval-Constant, M. Lacroix, K. Hortmann, O. V. Safonova and A. Y. Khodakov, *Chem. Commun.*, 2010, **46**, 788–790.
62 S. Bals, K. J. Batenburg, D. D. Liang, O. Lebedev, G. Van Tendeloo, A. Aerts, J. A. Martens and C. E. A. Kirschhock, *J. Am. Chem. Soc.*, 2009, **131**, 4769–4773.
63 I. Kasatkin, P. Kurr, B. Kniep, A. Trunschke and R. Schlogl, *Angew. Chem., Int. Ed.*, 2007, **46**, 7324–7327.
64 B. M. Weckhuysen, *Chem. Commun.*, 2002, 97–110.
65 A. Brückner, *Catal. Rev. Sci. Eng.*, 2003, **45**, 97–150.
66 S. J. Tinnemans, J. G. Mesu, K. Kervinen, T. Visser, T. A. Nijhuis, A. M. Beale, D. E. Keller, A. M. J. van der Eerden and B. M. Weckhuysen, *Catal. Today*, 2006, **113**, 3–15.
67 J. Becker, M. Bremholm, C. Tyrsted, B. Pauw, K. M. O. Jensen, J. Eltzholt, M. Christensen and B. B. Iversen, *J. Appl. Crystallogr.*, 2010, **43**, 729–736.
68 S. Nikitenko, A. M. Beale, A. M. J. van der Eerden, S. D. M. Jacques, O. Leynaud, M. G. O'Brien, D. Detollenaere, R. Kaptein, B. M. Weckhuysen and W. Bras, *J. Synchrotron Radiat.*, 2008, **15**, 632–640.
69 G. Artioli, T. Cerulli, G. Cruciani, M. C. Dalconi, G. Ferrari, M. Parisatto, A. Rack and R. Tucoulou, *Anal. Bioanal. Chem.*, 2010, **397**, 2131–2136.
70 K. Simmance, G. Sankar, R. G. Bell, C. Prestipino and W. van Beek, *Phys. Chem. Chem. Phys.*, 2010, **12**, 559–562.
71 A. Marcelli, D. Hampai, W. Xu, L. Malfatti and P. Innocenzi, *Acta Physica Polonica A*, 2009, **115**, 489–500.

72 M. A. Newton and W. vanBeek, *Chem. Soc. Rev.*, 2010, **39**, DOI: 10.1039/b919689g (this themed issue).
73 R. J. Davies, M. Burghammer and C. Riekel, *J. Synchrotron Radiat.*, 2009, **16**, 22–29.
74 T. Scheler, M. Rodrigues, T. W. Cornelius, C. Mocuta, A. Malachias, R. Magalhaes-Paniago, F. Comin, J. Chevrier and T. H. Metzger, *Appl. Phys. Lett.*, 2009, **94**, 023109.
75 K. Tiedtke, A. Azima, N. von Bargen, L. Bittner, S. Bonfigt, S. Dusterer, B. Faatz, U. Fruhling, M. Gensch, C. Gerth, N. Guerassimova, U. Hahn, T. Hans, M. Hesse, K. Honkavaar, U. Jastrow, P. Juranic, S. Kapitzki, B. Keitel, T. Kracht, M. Kuhlmann, W. B. Li, M. Martins, T. Nunez, E. Plonjes, H. Redlin, E. L. Saldin, E. A. Schneidmiller, J. R. Schneider, S. Schreiber, N. Stojanovic, F. Tavella, S. Toleikis, R. Treusch, H. Weigelt, M. Wellhofer, H. Wabnitz, M. V. Yurkov and J. Feldhaus, *New J. Phys.*, 2009, **11**, 023029.
76 W. A. Barletta, J. Bisognano, J. N. Corlett, P. Emma, Z. Huang, K. J. Kim, R. Lindberg, J. B. Murphy, G. R. Neil, D. C. Nguyen, C. Pellegrini, R. A. Rimmer, F. Sannibale, G. Stupakov, R. P. Walker and A. A. Zholents, *Nucl. Instrum. Methods Phys. Res., Sect. A*, 2010, **618**, 69–96.
77 A. Fouras, M. J. Kitchen, S. Dubsky, R. A. Lewis, S. B. Hooper and K. Hourigan, *J. Appl. Phys.*, 2009, **105**, 102009.
78 H. Yamada, T. Hiraia, M. Morita, D. Hasegawa and M. Hanashima, in *MIRRORCLE light source demonstrating one micron resolution and clear density mapping - art. no. 70780P*, ed. S. R. Stock, 2008.
79 M. M. Haque, H. Yamada, A. Moon and M. Yamada, *J. Synchrotron Radiat.*, 2009, **16**, 299–306.
80 R. L. Owen, J. M. Holton, C. Schulze-Briese and E. F. Garman, *J. Synchrotron Radiat.*, 2009, **16**, 143–151.

